THE 2013 RIM FIRE

Implications for Predicting Extreme Fire Spread, Pyroconvection, and Smoke Emissions

BY DAVID A. PETERSON, EDWARD J. HYER, JAMES R. CAMPBELL, MICHAEL D. FROMM, JOHNATHAN W. HAIR, CAROLYN F. BUTLER, AND MARTA A. FENN

One of the largest wildfires in California's history provides a unique opportunity to examine the meteorology driving extreme fire behavior and its impact on smoke plume altitude and downwind transport.

An illegal campfire ignited the Rim Fire on 17 August 2013 in the Stanislaus National Forest region of the Sierra Nevada. The Rim Fire eventually became the third largest wildfire in California history, burning more than 104,000 ha (http://cdfdata.fire.ca.gov/incidents/incidents_statsevents). This includes 30,000 ha in Yosemite National Park (Kirn and Dickman 2013), where the power and water supply to the San Francisco Bay Area became endangered. While old fire scars and prescribed burns reduced the fuel load in a portion of the region (e.g., Johnson et al. 2013), other sections had experienced substantial fuel accumulation resulting from many years of fire suppression activity. The combination of topography, remoteness, and meteorological conditions contributed to the 1.5-month lifetime of the fire, marked by occasional rapid fire spread and significant variations in smoke plume physical characteristics. These topics serve as motivation for this article, which provides a comprehensive overview, focusing on the most extreme fire behavior, its atmospheric interaction, and the efficacy of specific parameters for improving predictive capabilities in North America.

Large wildfire events similar to the Rim Fire are an increasingly common threat to life and property across the western United States (e.g., Westerling et al. 2006; Dennison et al. 2014). In addition, aerosol and trace gas production, by-products of wildfire activity, are increasingly recognized as threats to regional air quality, visibility, and even global climate (e.g., Randerson et al. 2006; Spracklen et al. 2007; Salinas et al. 2013; Val Martin et al. 2013). As a result, several near-real-time global and regional smoke forecasting applications have been developed to support decision making by civil authorities. Examples of this include

AFFILIATIONS: PETERSON—National Research Council, Washington, D.C., and Naval Research Laboratory, Monterey, California; HYER AND CAMPBELL—Naval Research Laboratory, Monterey, California; FROMM—Naval Research Laboratory, Washington, D.C.; HAIR—NASA Langley Research Center, Hampton, Virginia; BUTLER AND FENN—Science Systems and Applications Inc., and Langley Research Center, Hampton, Virginia
CORRESPONDING AUTHOR: David Peterson, National Research Council Postdoctoral Fellow, Naval Research Laboratory, 7 Grace Hopper Avenue, Monterey, CA 93943
E-mail: david.peterson.ctr@nrlmry.navy.mil

The abstract for this article can be found in this issue, following the table of contents.
DOI:10.1175/BAMS-D-14-00060.1

In final form 16 October 2014

the Fire Locating and Modeling of Burning Emissions (FLAMBE), developed by the U.S. Naval Research Laboratory (Reid et al. 2009); the Fire Inventory from NCAR (FINN) (Wiedinmyer et al. 2011); the BlueSky Smoke Modeling Framework, produced by the U.S. Forest Service (Larkin et al. 2009); the Global Fire Emissions Database (GFED) (van der Werf et al. 2010; Mu et al. 2011); the Global Fire Assimilation System (GFAS) (Kaiser et al. 2012); and the global biomass burning emission product produced by the National Oceanic and Atmospheric Administration (Zhang et al. 2008, 2012).

Within these systems, smoke emission distributions are driven by the spatiotemporal patterns of satellite-based fire observations that form input parameterizations. However, for numerical forecasting of smoke transport, it is typically assumed that observed fire activity does not change throughout the forecast period. While a "persistence forecast" may exhibit skill in certain fire regimes (e.g., the African Sahel; Giglio et al. 2006), it yields poor smoke emissions forecasts in the mid- and upper latitudes (e.g., Reid et al. 2009), which experience large intraseasonal meteorological variability (e.g., Flannigan and Harrington 1988; Mu et al. 2011; Peterson et al. 2013a). Operational fire weather forecasts in these environments usually depend on a variety of indices derived from local surface observations (e.g., Van Wagner 1987; Haines 1988; Werth and Ochoa 1993; Amiro et al. 2004; Potter et al. 2008). Recently, several fire weather indices have been modified to work with numerical weather prediction (NWP) inputs (e.g., Mölders 2008; Simpson et al. 2014). Peterson et al. (2013a) show how fire weather indices incorporated into regional weather models help distinguish days of fire growth from those with fire decay, thus improving on a persistence forecast. However, standard fire weather indices may have limited capability for identifying the most extreme fire spread events.

The vertical profile of wildfire smoke distribution near the source is also highly variable (e.g., Kahn et al. 2007, 2008; Val Martin et al. 2012; Peterson et al. 2014), which can drastically impact the extent of downwind transport. Many smoke plumes are confined to the boundary layer, compromising visibility and air quality locally. However, if a plume reaches the free troposphere, its atmospheric residence time increases, allowing smoke particles to be transported thousands of kilometers (e.g., Westphal and Toon 1991; Wotawa and Trainer 2000; Damoah et al. 2006; Duck et al. 2007; Hyer et al. 2007). Air quality and visibility, therefore, can be negatively affected at locations far downwind of the source (e.g., Sapkota et al. 2005; Wang et al. 2006, 2013; Dempsey 2013; Campbell et al. 2015, unpublished manuscript), including central Canada during the Rim Fire (http://alg.umbc.edu/usaq/archives/2013_08.html).

Complicating conceptual models for the vertical distribution of smoke particles, especially in the middle and upper latitudes, is the impact from pyrocumulus (pyroCu) clouds, which were observed on many days during the Rim Fire. At least two fire-triggered thunderstorms, known as pyrocumulonimbus (or pyroCbs, http://glossary.ametsoc.org/wiki/Pyrocumulonimbus), were also observed. Recent studies have highlighted the ability of pyroCbs to inject smoke into the upper troposphere or even lower stratosphere (e.g., Fromm et al. 2010, 2012), where wildfires are a key source of particulate intrusions. However, the meteorological conditions driving large pyroCbs are still uncertain, and an automated regional pyroCb prediction system has not been developed.

With its long lifetime and high frequency of extreme fire behavior, the 2013 Rim Fire (http://inciweb.nwcg.gov/incident/3660/#) provides a unique opportunity to identify the key meteorological conditions and fire characteristics driving both extreme fire spread and pyroCb events. A wide variety of ground, airborne, and spaceborne observations are employed in this pursuit, including aircraft observations from the NASA Studies of Emissions and Atmospheric Composition, Clouds and Climate Coupling by Regional Surveys (SEAC^{4}RS) field mission (https://espo.nasa.gov/home/seac4rs/). Using these resources, the limitations of traditional fire weather indices and conflicting hypotheses surrounding pyroCb development are examined. Variations in smoke plume altitude and transport are also explored. This analysis of the Rim Fire is an important step toward improving methodologies currently used for regional fire weather, air quality, and visibility forecasts.

FIRE EVOLUTION FROM AIRBORNE AND SATELLITE OBSERVATIONS. Using nightly airborne observations, the U.S. Forest Service (USFS) National Infrared Operations (NIROPS) provides fire perimeter maps and burned area estimates for many fire events, especially when there is an immediate risk to life and property (http://nirops.fs.fed.us/). NIROPS analyses were posted at an irregular schedule during the Rim Fire, generally between 0400 and 1000 UTC [2100–0300 local time (LT)]. Figure 1 displays the estimated daily fire

progression based on the NIROPS observation closest to local midnight each day. Steady growth was observed for the first two days (17–18 August), with the fire front generally spreading in all directions. On 19 August, the front was displaced noticeably to the south. By 20 August, the direction of spread shifted to the east-northeast and the rate of spread increased further, exploding in relative size during the evening of 21 August. As shown in Fig. 2 (red curve), this period of extreme fire spread (spread event 1) persisted through 23 August, burning 36,206 ha (~35% of the total burned area). A second significant spread event (spread event 2) began during the evening of 25 August, and burned 12,067 ha (~12% of the total) by the evening of 26 August.

Several spaceborne sensors have fire detection capabilities, and are typically used in combination with (or in place of) NIROPS burned area estimates. The Geostationary Operational Environmental Satellites (GOES; Prins and Menzel 1994; Prins et al. 1998) and the twin Moderate Resolution Imaging Spectroradiometer (MODIS) sensors (Giglio et al. 2003; Giglio 2010), flown aboard NASA's *Terra* and *Aqua* satellites, are prominent examples. Differences in orbit and spatial resolution allow MODIS (~1-km resolution) to detect smaller fires than GOES (~4-km resolution) but with less frequent observations, which can result in both random and systematic errors in reconstructed fire time series (Hyer et al. 2013). During the Rim Fire, three GOES sensors provided observations at least every 15 min. However, the operational GOES sensor observing western North America (GOES-West, currently *GOES-15*) and occasional 1-min data from *GOES-14* were the most relevant. In addition to fire detection, sensors like GOES can also be used to estimate instantaneous fire radiative power (FRP, in MW), which provides information on the radiant heat output of detected fires and is commonly used as a proxy for fire intensity (e.g., Kaufman et al. 1998; Giglio et al. 2003; Wooster et al. 2003).

The GOES FRP calculation is based on the brightness temperature (or radiance) difference between the pixel containing fire and the surrounding nonfire region in the middle infrared (~4 μm, GOES channel 2; Wooster et al. 2005; Schroeder et al. 2010). To create a consistent and representative time series, observations from GOES-West were accumulated

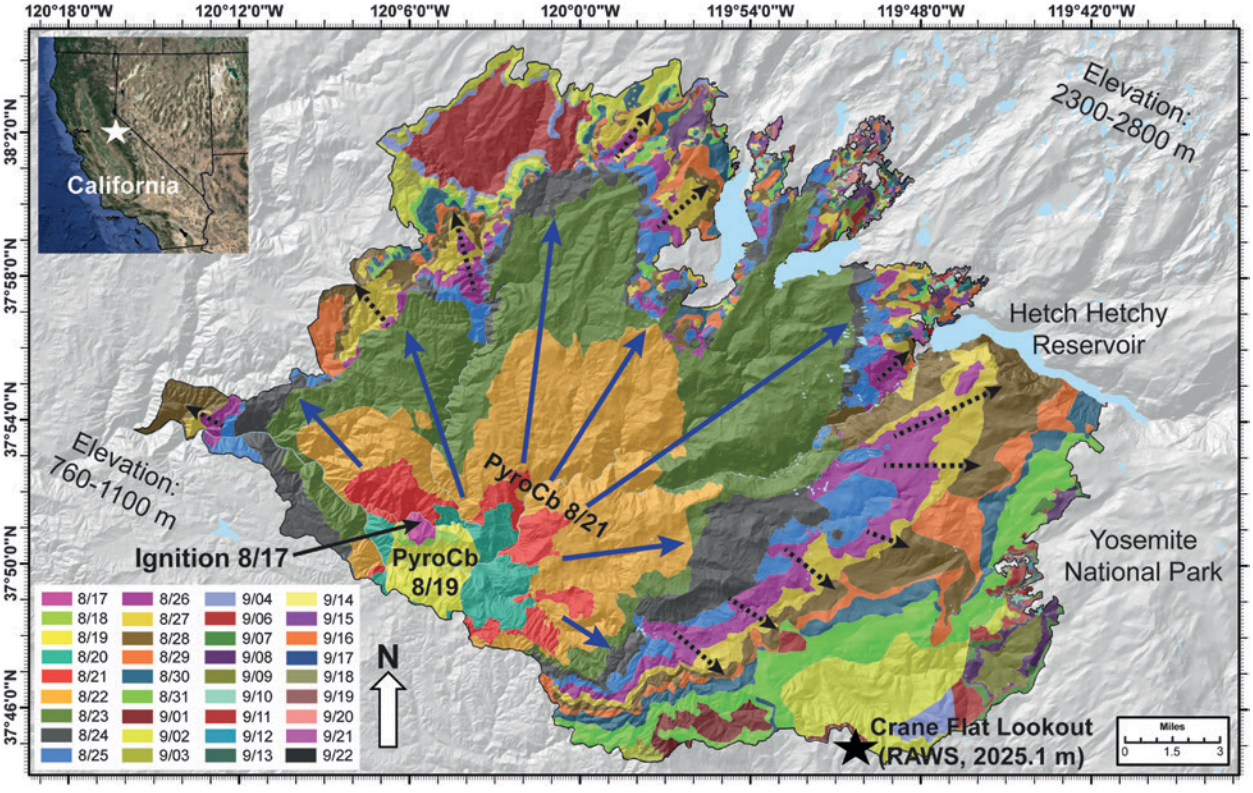

Fig. 1. Rim Fire map, with color scheme indicating the USFS-estimated daily fire progression based on the NIROPS observation closest to 0700 UTC (midnight LT) for 17 Aug–22 Sep 2013. Solid blue and dashed black arrows indicate the approximate area burned during spread events 1 and 2, respectively.

hourly and the total retrieved instantaneous FRP over the Rim Fire area was divided by the number of available observations per hour. For fire pixels where no valid FRP could be retrieved, either the mean hourly per-pixel FRP or the mean per-pixel FRP over the fire lifetime was substituted. The resulting normalized FRP time series is displayed in Fig. 2 (black curve), showing a distinct, meteorology-driven diurnal fluctuation in FRP that oscillates between maxima in late evening and minima in the morning. All satellite FRP data can be compromised by opaque cloud cover. However, the majority of the Rim Fire time series was marked by mostly clear or partly cloudy conditions. The only exceptions were intermittent convection during the first few days of the fire (17–21 August; note that FRP measurements during PyroCb events will be compromised) and thick synoptic cloud cover at the end of the time series (21 September). During intense fire events, GOES FRP may also be underestimated due to occasional saturation of the sensor.

The Rim Fire's primary burning period of 17–31 August was marked by the largest observed fire spread, frequently coinciding with hourly FRP values above 4,000 MW (Fig. 2). This implies that FRP may be related to changes in area burned. Recent studies have also shown that FRP is proportional to fuel consumption and smoke emission rates (e.g., Wooster 2002; Wooster et al. 2003, 2005; Ichoku and Kaufman 2005; Roberts et al. 2005, 2009; Ichoku et al. 2008a,b; Jordan et al. 2008). In addition, FRP variations have been linked to measures of burn severity (e.g., Heward et al. 2013), indicating that the peaks in FRP observed during the Rim Fire likely coincide with the most intense and severe burning. Moreover, the combination of high FRP and weaker atmospheric stability generally leads to higher-altitude smoke plumes and a greater chance of smoke injection and transport within the free troposphere (e.g., Val Martin et al. 2010; Peterson et al. 2014).

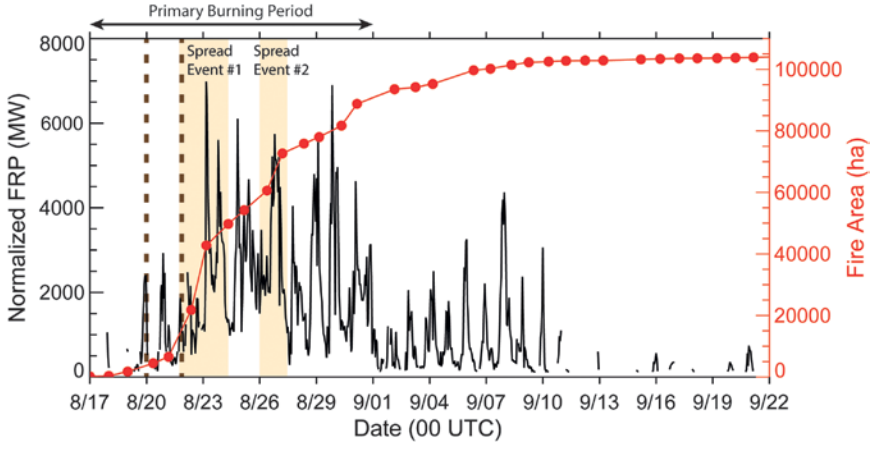

Fig. 2. Time series of normalized hourly FRP from GOES-West (black) and cumulative fire area based on nighttime NIROPS observations (red). Spread events 1 and 2 are highlighted with yellow shading, and the pyroCb events of 19 and 21 Aug are denoted by dashed brown vertical lines.

GENERAL METEOROLOGY OF THE RIM FIRE.

Much of California experienced below-average precipitation during its primary wet season (November–March) of 2012/13, especially after 1 January 2013. During the months and weeks preceding ignition, the region continued to experience both long-term and short-term drought (http://droughtmonitor.unl.edu/MapsAndData/MapArchive.aspx), resulting in very dry fuel conditions. The intense burning and rapid spread observed during the primary burning period of 17–31 August generally coincided with warm temperatures and relative humidity (RH) values below 40% each afternoon. However, several key changes in local meteorology were also observed.

During the first few days of the fire, a large portion of California was under the influence of a broad upper-level low that became cut off from the mean synoptic flow in the days preceding ignition (Fig. 3a). The North American Regional Reanalysis (NARR; http://nomads.ncdc.noaa.gov/data.php#narr_datasets; Mesinger et al. 2006) shows that the center of the low was located off the Southern California coastline on the first day of burning (18 August), and low-level winds (850 hPa) were light and southeasterly near the Rim Fire. As is typical with large cutoffs, the low then began to retrograde (e.g., Holton 2004), causing low-level winds near the fire to shift more northerly by the evening of 19 August (Fig. 4a). This directed the fire front to the south, or generally downhill (Fig. 1). During 20–22 August, the low progressed back toward California, causing low-level winds to become southwesterly (Figs. 4b–d), redirecting the fire to the northeast along generally uphill slopes (Fig. 1). As near-surface pressure gradients increased between the low and an inland ridge, wind

speeds increased from 3 m s^{-1} (5 kt) to 8–10 m s^{-1} (15–20 kt). This combination of stronger winds in a general uphill and up-canyon direction very likely increased the rate of fire spread.

Relatively cold upper-tropospheric air associated with the cutoff low provided sufficient instability for scattered convection and some precipitation in the higher terrain near the fire. The two pyroCb events also occurred during this period, on 19 and 21 August. Convective activity then diminished as the cutoff low merged with a broad synoptic trough approaching the Pacific Northwest. Southwesterly synoptic flow on the eastern side of the trough pushed the low onshore and ejected it through central California between 21 and 22 August (Fig. 3a). The digging trough also maintained a strong pressure gradient over central California, producing strong surface winds (Fig. 4d). This coincides with the rapid uphill fire spread observed during spread event 1 (Fig. 1), marked by the largest increases in area burned and the highest FRP values (Fig. 2).

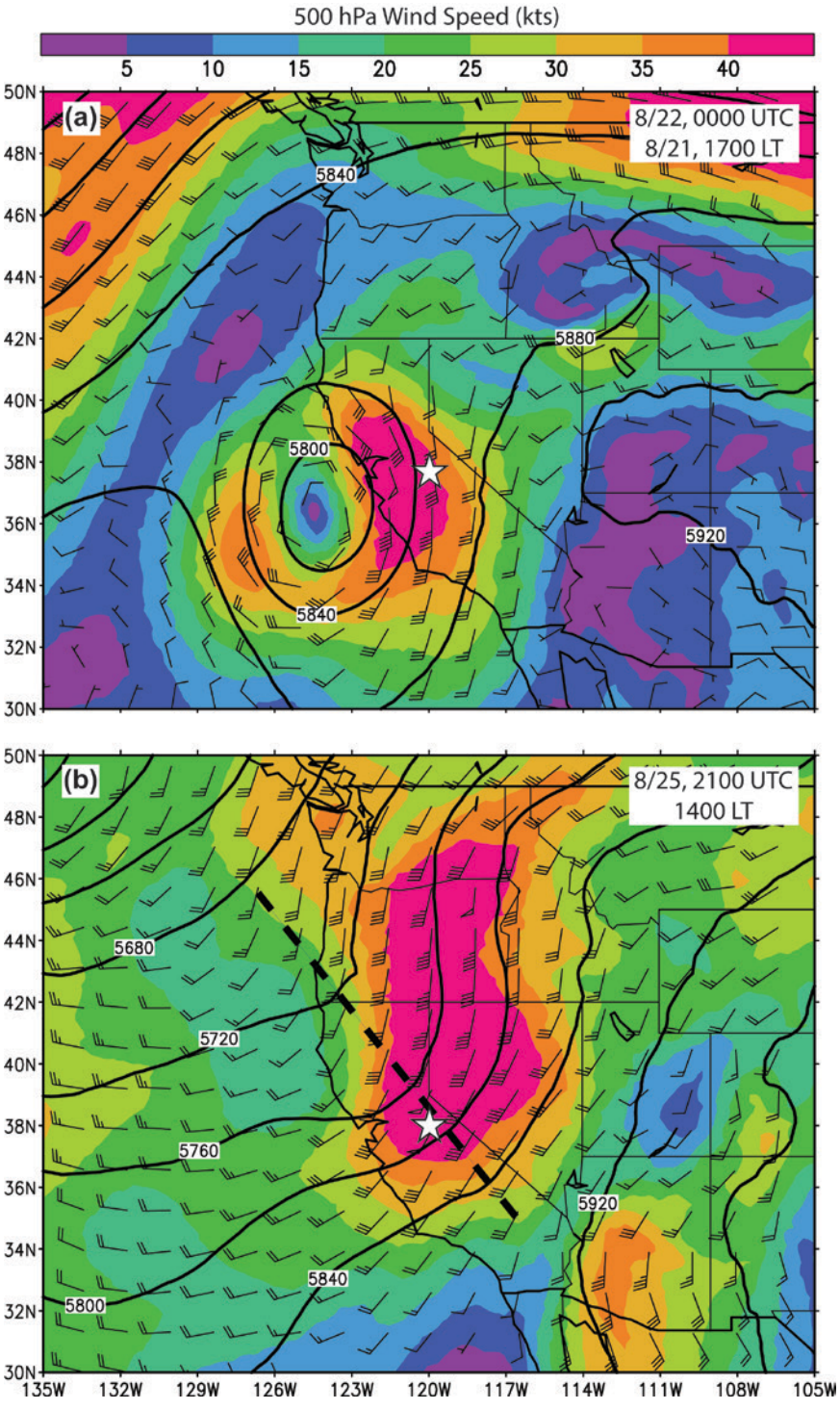

Fig. 3. NARR 500-hPa heights (contoured every 40 m) and wind barbs (kt) for (a) 0000 UTC 22 Aug 2013 (1700 LT 21 Aug) and (b) 2100 UTC 25 Aug (1400 LT). Shading indicates the 500-hPa wind speed, and the white star denotes the location of the Rim Fire. The dashed black line in (b) indicates the axis of the shortwave trough.

During 24 August and part of 25 August, the Rim Fire's growth slowed and FRP decreased (Figs. 1, 2). This was largely influenced by increasing RH, reduced wind speed, and the lowest surface temperatures observed during the primary burning period. While the air temperature was lower, the passage of a shortwave trough (Fig. 3b) caused low-level wind speeds to increase again during the afternoon and evening of 25 August, coinciding with the initiation of spread event 2.

By the end of August, temperatures warmed and RH values reached another relative minimum.

However, surface wind conditions were not as favorable as during the major spread events. Portions of the fire were also becoming increasingly contained, either by fire suppression teams or natural barriers. As a result, extreme fire spread did not occur. Burning continued through 10 September at a slower rate of spread than the primary burning period (Figs. 1, 2). During 11–21 September, FRP dropped significantly and very slow growth was observed. The first substantial (>12 mm) synoptic rainfall occurred on 21–22 September, effectively ending the satellite fire detection record for the Rim Fire (Fig. 2). However, smoldering and occasional weak flare-ups continued into early October.

PRIMARY DRIVERS OF EXTREME FIRE SPREAD. A variety of fire weather indices are currently available to forecast the potential for "extreme fire danger" across North America. In the continental United States (CONUS), regional fire weather forecasts commonly employ the Haines index: an integer scale (1–6) based on two equally weighted ingredients for moisture and stability derived from a lower-level (850 or 700 hPa) dewpoint depression and lower-atmospheric lapse rate, respectively (Haines 1988; Potter et al. 2008). The specific pressure levels used for the Haines index calculations vary, depending on local topography.

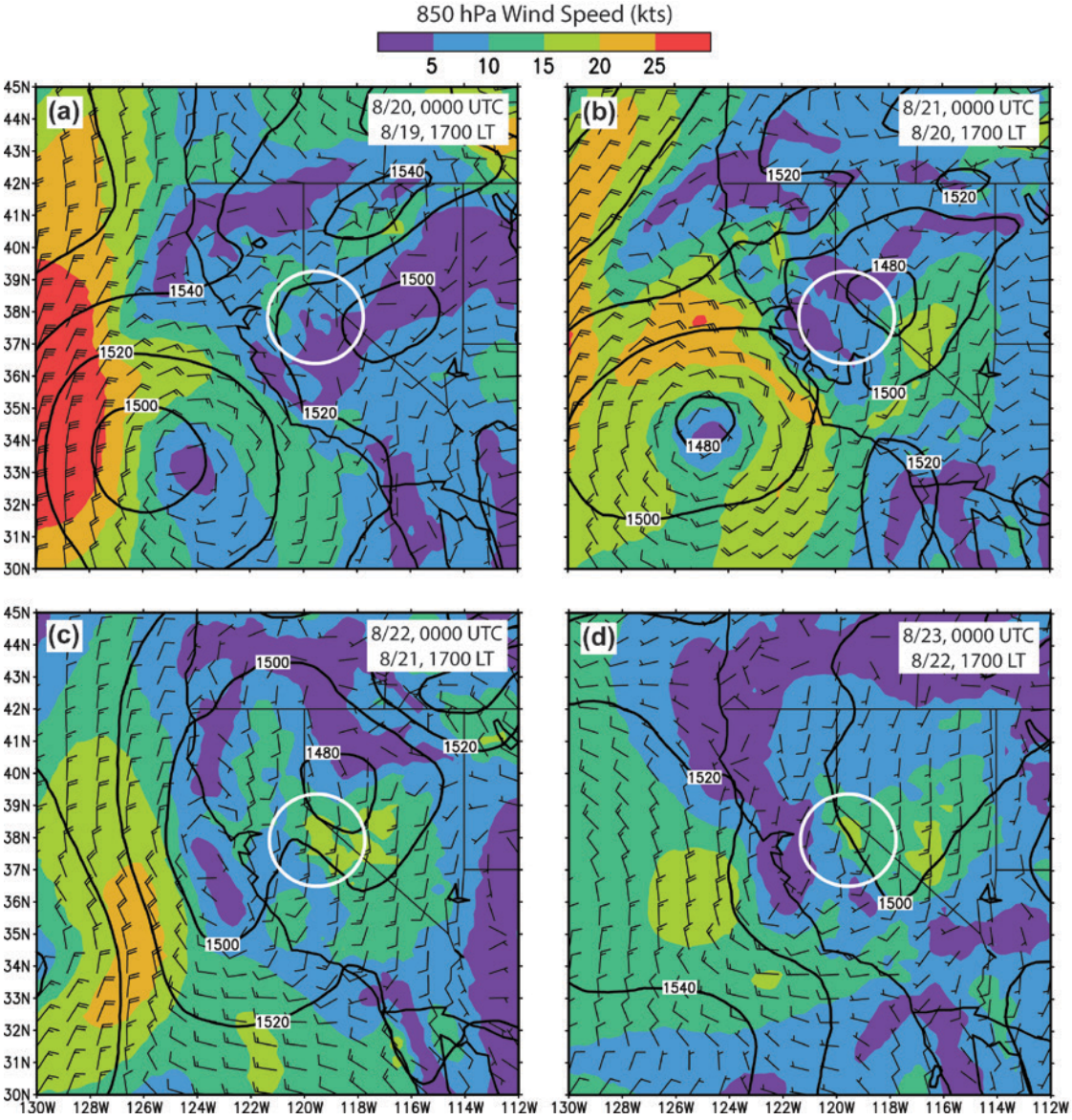

Fig. 4. NARR 850-hPa heights (contoured every 20 m) and wind barbs (kt) for (a)–(d) 0000 UTC 20–23 Aug 2013 (1700 LT 19–22 Aug). Shading indicates the 850-hPa (near surface) wind speed, and the white circle denotes the primary study region.

The majority of the Rim Fire's primary burning period, including spread events 1 and 2, was marked by a dry lower troposphere, with a low-level thermal lapse rate near dry adiabatic. As a result, all fire weather indices, including the Haines index, indicated maximum fire danger (value of 6) nearly every afternoon. Figure 5 highlights the high Haines index environment on the first afternoon of spread event 1 (22 August), using the NARR-derived sounding for the Rim Fire coincident with the *Aqua* MODIS overpass at 2130 UTC (1430 LT). The upper limit of the Haines index can be extended for increased sensitivity to the most extreme fire danger (Mills and McCaw 2010). However, this "continuous Haines index" also produced values near the 95th percentile of fire danger (value of ~8–10). Therefore, lower-atmospheric fire weather indices, such as the Haines index, lack the fidelity for distinguishing days with extreme fire spread from those with more gradual spread.

During the Rim Fire, the largest spread and FRP was generally initiated as an upper-level disturbance passed over (or near) the fire (Fig. 3). A similar link has been highlighted by previous studies (e.g., Brotak and Reifsnyder 1977; Westphal and Toon 1991; Werth and Ochoa 1993). The impact on surface wind speed and RH is examined in Fig. 6, using hourly observations from the remote automatic weather station (RAWS, www.raws.dri.edu/wraws/ccaF.html) at Crane Flat Lookout (37.76°N, 119.82°W, elevation of 2,025.1 m, 6,644 ft; Fig. 1). These data confirm that spread event 1 coincided with some of the strongest hourly wind speeds (>5 m s^{-1}) and lowest RH values (<30%) observed during the primary burning period. Figure 6 also displays daytime and nighttime means for each respective parame-

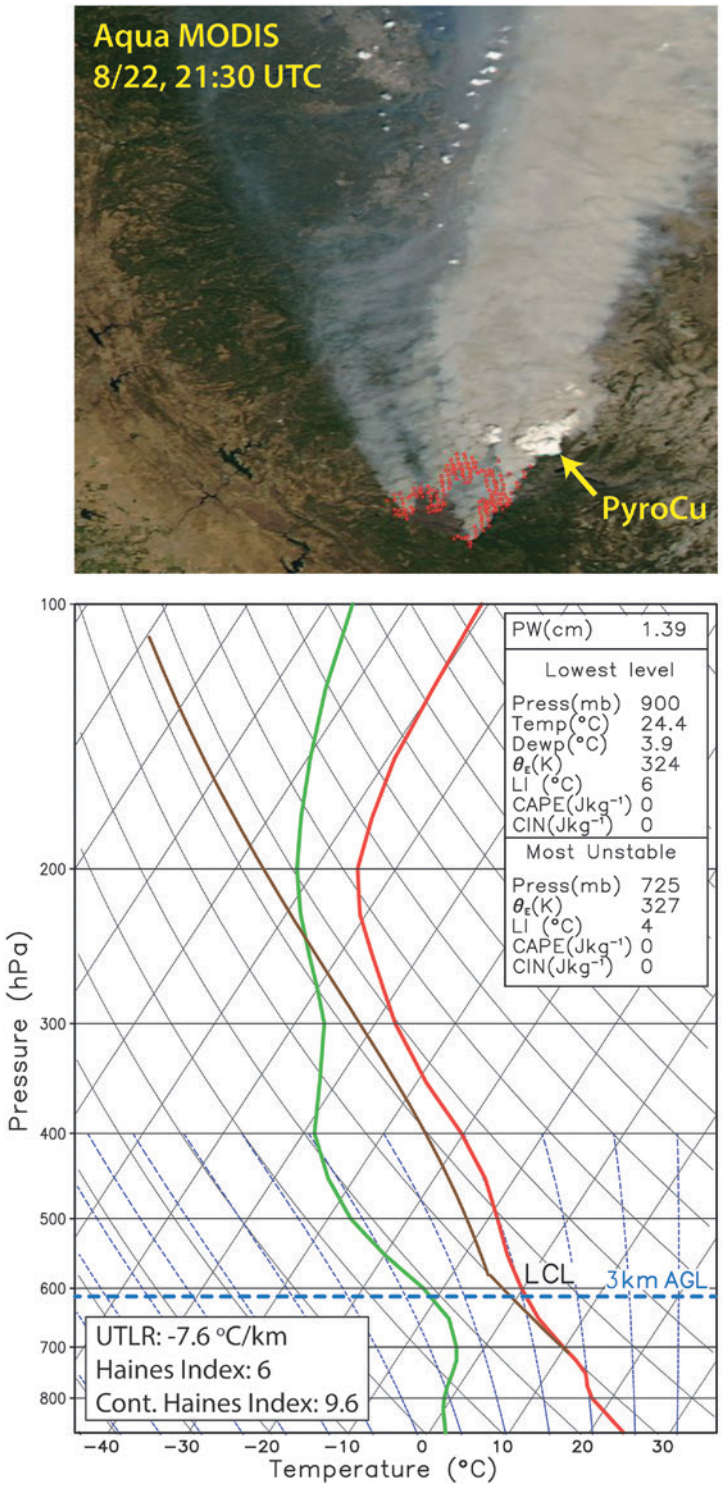

Fig. 5. (top) *Aqua* MODIS true color image on 22 Aug 2013 (spread event 1) with fire pixels displayed in red and (bottom) the corresponding NARR sounding at 2100 UTC (1430 LT), derived from the NARR grid box closest to the RAWS station used in Fig. 6. Red and green profiles in the sounding correspond to environmental temperature and dewpoint, respectively. The brown parcel path corresponds to the most unstable parcel. Dashed blue horizontal line indicates the typical extent of vertical mixing each afternoon (~3 km) during the primary burning period.

ter, using the hours of 1600–0300 UTC (0900–2000 LT) and 0400–1500 UTC (2100–0800 LT).

During a typical diurnal cycle, low-level wind speeds will decrease and RH will increase during the nighttime and early morning hours, lowering fire danger and minimizing overall activity (Giglio 2007; Ichoku et al. 2008a; Mu et al. 2011). However, spread event 1 was marked by the highest nighttime mean wind speed (~3.7 m s^{-1}) and two consecutive nights with a mean RH below 35%. Furthermore, winds generally remained southerly, and thus uphill, for many of the nighttime hours. The combination of these factors likely enabled FRP to remain high during these nights (>1,000 MW, Fig. 2), which likely enhanced extreme fire spread.

Spread event 2 likely initiated during the evening of 25 August from the increase in surface wind speed associated with the passage of the aforementioned shortwave trough (Fig. 6, brown vertical line). Mean surface wind speeds during the nighttime period between 25 and 26 August were similar to spread event 1 (~3.5 m s^{-1}), persisting through the daytime hours on 26 August. Some of the strongest wind gusts observed during the primary burning period (9–13 m s^{-1}, not shown) also occurred during spread event 2. However, the corresponding mean RH was higher than spread event 1 (43% nighttime, 33% daytime). When considering these offsetting variations in wind speed and RH, it is not surprising that FRP and area burned were lower than spread event 1.

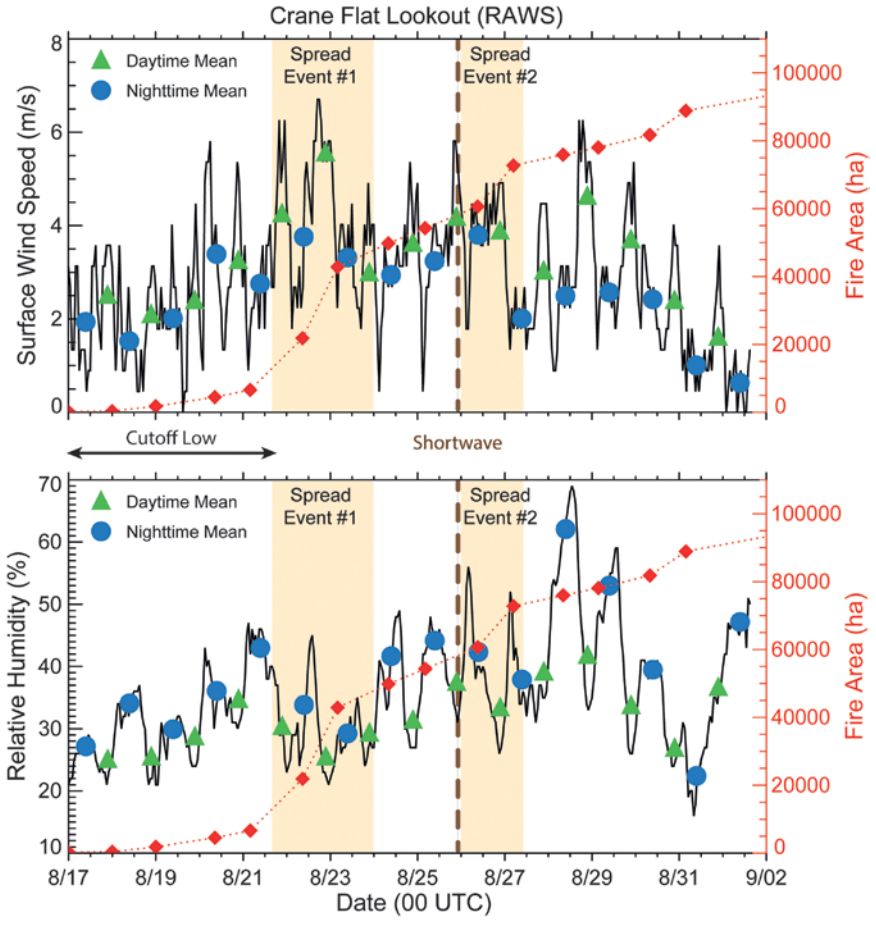

Fig. 6. Primary burning period surface observations (black curve) of (top) hourly mean wind speed and (bottom) RH from the RAWS station at Crane Flat Lookout (www.raws.dri.edu/cgi-bin/rawMAIN.pl?caCCRA), located within Yosemite National Park (Fig. 1). Daytime (green triangles) and nighttime means (blue circles) were calculated using the hours of 1600–0300 UTC (0900–2000 LT) and 0400–1500 UTC (2100–0800 LT), respectively. The time series of cumulative fire area based on nighttime NIROPS observations is displayed in red. Spread events 1 and 2 are highlighted with yellow shading, and the approximate time of the shortwave passage (25 Aug, evening) is denoted by the dashed brown vertical line.

The combination of fuel characteristics, topography, and meteorology, including the daytime and nighttime variations highlighted in Fig. 6, are usually an important consideration for incident meteorologists and finescale modeling of individual fires (e.g., Coen and Schroeder 2013). However, as mentioned above, regional and global forecasts are largely based on the available suite of fire weather indices, which represent more broad-scale conditions. Many of these indices do not distinguish between daytime and nighttime meteorology, and several are based explicitly on daytime conditions (e.g., Van Wagner 1987). Fire weather indices also lack the flexibility to account for disturbances in the upper levels of the troposphere (e.g., 500 hPa), where NWP analyses and forecasts are more stable. Therefore, automated prediction of extreme spread potential on a regional level will likely require a top-down approach, similar to the

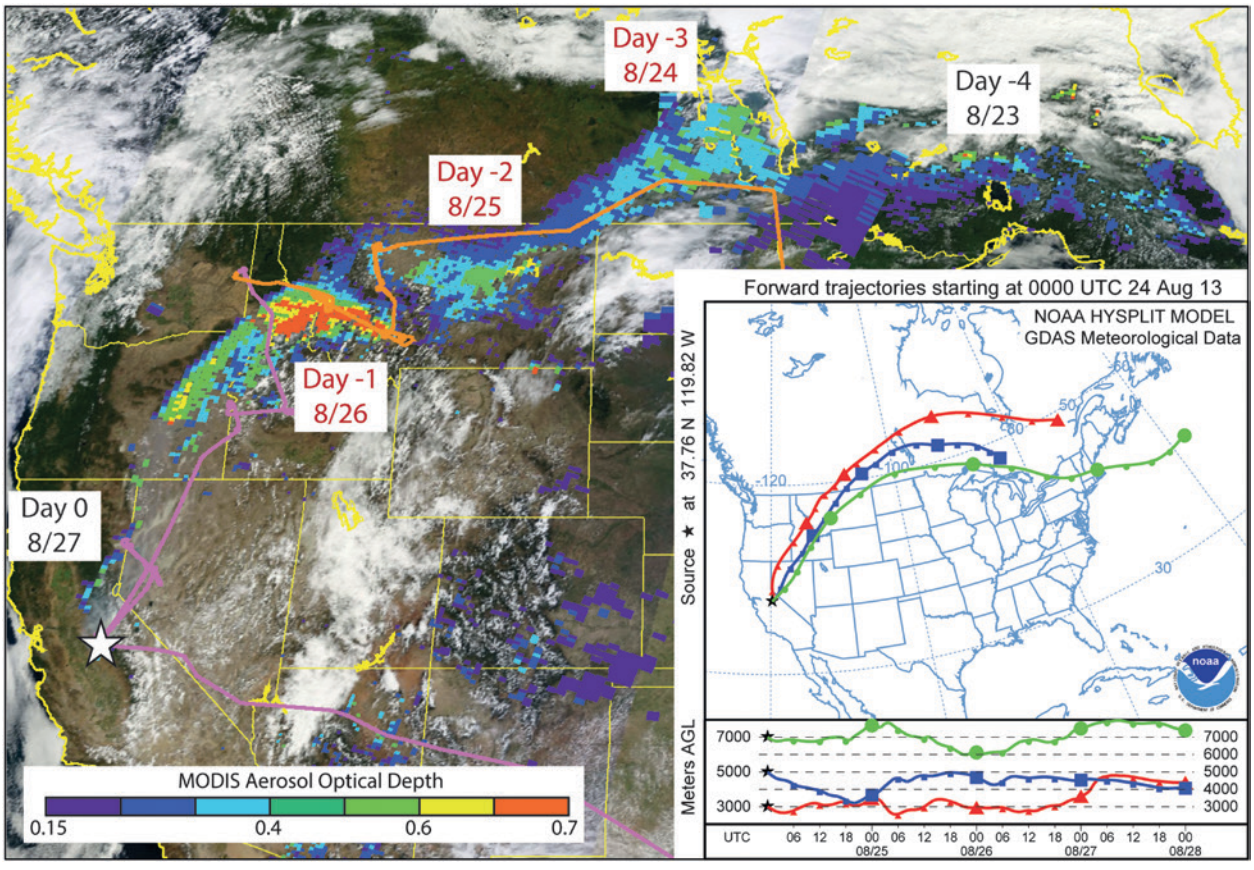

Fig. 7. *Terra* MODIS true color imagery for the morning of 27 Aug 2013, with valid AOD (MOD04_L2) retrievals superposed. The relevant segments of the NASA DC-8 flight paths on 26 Aug (Houston, TX, to Spokane, WA) and 27 Aug (Spokane to Houston) are highlighted in pink and orange, respectively. The inset image displays forward HYSPLIT trajectories initialized at 0000 UTC 24 Aug (1700 LT 23 Aug) for smoke particles injected at 3 (red), 5 (blue) and 7 km (green) AGL. The 3- and 5-km trajectories are used to identify the approximate date associated with each pulse of smoke in the larger MODIS image. Dates in red correspond to at least some of the smoke sampled by the two DC-8 flights (~48–50 h of smoke emissions).

"forecast funnel" methodology employed in operational weather forecasting (Snellman 1982).

SMOKE PLUME CHARACTERISTICS DURING EXTREME FIRE SPREAD. Given a high Haines index environment, the Rim Fire likely initiated a positive feedback loop, where high FRP produced a strong, unimpeded convective column that increased the entrainment of air near the fire, generating higher FRP and potentially a faster rate of spread. This situation is commonly referred to as a "plume-dominated fire," where the fire is creating and sustaining its own favorable weather conditions (e.g., Rothermel 1991; Werth and Ochoa 1993). Plume-dominated fires are also favorable for development of pyroCu, high-altitude smoke injections, and relatively long-distance smoke transport. As evidenced by capping pyroCu in the MODIS imagery (Fig. 5), the Rim Fire's largest spread events may actually be considered a hybrid plume-dominated fire, driven by a combination of smoke plume effects (high Haines index) and the aforementioned synoptic, mesoscale, and nocturnal meteorology.

During both spread events, smoke particles were generally transported to the north or northeast around a large area of high pressure in the central CONUS. *Terra* MODIS aerosol optical depth (AOD) (MOD04_L2; e.g., Remer et al. 2005) retrieved at ~1030 LT 27 August depicts a broad fetch of elevated values originating near the Rim Fire and reaching well into central Canada (Fig. 7). The Rim Fire smoke plume was also sampled intermittently by the NASA DC-8 aircraft as part of the SEAC^{4}RS field mission. Flight tracks are overlaid on Fig. 7. The first on 26 August (pink) observed the plume from the source region through central Idaho. The second flight, on 27 August (orange), sampled the plume from Idaho into central Canada. To some extent,

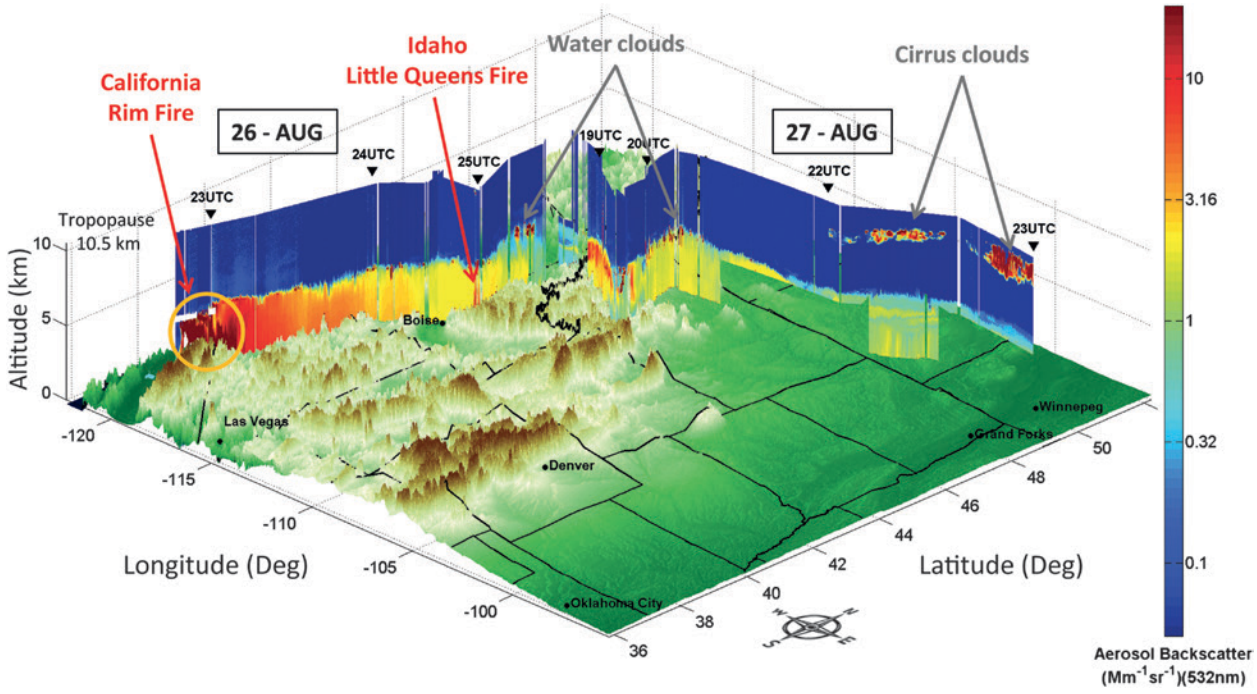

Fig. 8. Atmospheric backscatter observed by DIAL/HSRL from the surface to the mean height of the tropopause (10.5 km) during the two Rim Fire DC-8 flights on 26 and 27 Aug 2013. The up- and down-viewing DIAL/HSRL data have been interpolated across the region near the aircraft (500 m above and below the aircraft) where retrievals are not possible. Down-viewing data were unavailable when the aircraft flew at lower altitudes over portions of Canada.

smoke associated with decaying Idaho wildfires became mixed with the Rim Fire plume as it reached into Montana and Canada. However, with unfavorable fire weather conditions in this region, the plume sampled by the DC-8 was likely primarily composed of Rim Fire smoke.

The vertical distribution of Rim Fire smoke particles is displayed in Fig. 8 using aerosol backscatter from NASA's combined ozone differential absorption lidar (DIAL; Browell et al. 1998) and high spectral resolution lidar (HSRL; Hair et al. 2008). Smoke particles were well mixed from the surface to a weak stable layer at 3–5 km above ground level (AGL), with the highest backscatter near the fire. Observed and NARR-derived soundings reveal that the hot and dry low-level environment allowed for similar mixed-layer depths on many afternoons during the primary burning period, typically near 3 km AGL (Fig. 5), but occasionally approaching 5 km AGL in portions of western Nevada and Idaho. As a result, the majority of smoke transport remained within the mixed layer. However, the DIAL/HSRL does indicate a slight increase in backscatter between 5 and 7 km AGL near the fire (Fig. 8), which is likely a result of diffuse smoke particles lofted during sporadic periods of pyroCu formation.

Forward trajectories from the National Oceanic and Atmospheric Administration (NOAA) Air Resources Laboratory (ARL) Hybrid Single-Particle Lagrangian Integrated Trajectory (HYSPLIT) model (www.arl.noaa.gov/HYSPLIT_info.php; Draxler and Rolph 2013) show that smoke particles injected between 3–5 km AGL at 0000 UTC 24 August (1700 LT 23 August) would have reached into central Canada by the morning of 27 August (Fig. 7). Therefore, the AOD map in Fig. 7 likely contains smoke particles emitted over a 4–5-day period (23–27 August), including the end of spread event 1 and most of spread event 2. However, any diffuse particle mass reaching as high as 7 km AGL would have reached the northern Atlantic Ocean during the same time period.

When considering a lag of ~16 h between the two flight paths, the DIAL/HSRL likely sampled smoke particles emitted over a shorter ~48–50-h period during 24–26 August, which coincides with smoke released prior to and during spread event 2. Figure 8 shows that the altitude of smoke particle injection and propagation remained at 3–5 km AGL (~700–500 hPa), despite the increase in FRP and burned area during this period. In addition, radiosonde profiles along the path of the smoke plume reveal a tropopause height near 10.5 km AGL, which

is well above the maximum observed plume height. Therefore, analysis of the Rim Fire indicates that extreme FRP alone is unlikely to correlate with smoke particles lofted to the top of the troposphere. Future studies will use the SEAC^{4}RS dataset obtained during the Rim Fire, and other 2013 fire events, for a more detailed examination of smoke plume composition and evolution in downwind regions.

TOWARD THE PREDICTION OF INTENSE PYROCONVECTION. While capping pyroCu and midtropospheric smoke particles are observed with many large fire events, the development of a pyroCb requires a large release of latent heat within the convective (smoke) plume. All wildfires release water vapor as a by-product of combustion, but the potential for entrainment of ambient moisture into the smoke plume must also be considered. Recent modeling studies have supported conflicting interpretations of this mechanism. Several studies suggest that latent heat production from combustion is a key driver of plume dynamics (e.g., Potter 2005), and entrainment of ambient moisture is relatively unimportant (Cunningham and Reeder 2009). In contrast, other studies show that sensible/radiant heat release is generally the key driver of plume dynamics (Luderer et al. 2009), and that the contribution of water vapor released during combustion decreases rapidly with height (Trentmann et al. 2006). This suggests that entrainment of water vapor in the midlevels is likely the primary driver of pyroCb development (Trentmann et al. 2006).

During the early days of the Rim Fire (17–21 August), including the two pyroCb events (19 and 21 August), RH values frequently exceeded 60% in the 650–450-hPa layer, but the lower troposphere remained dry (Fig. 9). As a result, NARR-derived soundings at the Rim Fire (Fig. 10) display more of an "inverted V" profile compared to spread event 1 (Fig. 5). Typical of high-based thunderstorms in the western CONUS, this midlevel moist layer supported the development of nonfire-related convection in the high terrain near the fire each afternoon (Fig. 10). However, dry conditions in the lower troposphere caused some of the precipitation to evaporate before reaching the ground. PyroCb development was therefore associated with conditions favorable for high-based, dry thunderstorms (<2.5 mm of rainfall), which require ambient midlevel moisture.

By definition, dry thunderstorms require a dry and unstable lower troposphere (high Haines index), but upper-level conditions must also be conducive for development. In California, dry thunderstorms typically develop ahead of an approaching trough, in a region with broad southwesterly synoptic flow that allows for advection of monsoonal moisture in the midtroposphere (e.g., Rorig and Ferguson 1999; Nauslar et al. 2013). This elevated moist layer must also be conditionally unstable, corresponding to an upper-tropospheric lapse rate (UTLR, 500–300 hPa) $\leq -7.5°C\ km^{-1}$. In addition, upper-level dynamics must be favorable for rising motion, usually associated with an ageostrophic jet streak circulation, and marked by divergence at 250 hPa (Wallmann et al. 2010; Nauslar et al. 2013). As highlighted in Fig. 10, the Rim Fire's two pyroCb events were indeed located ahead of an approaching cutoff low, producing an UTLR near

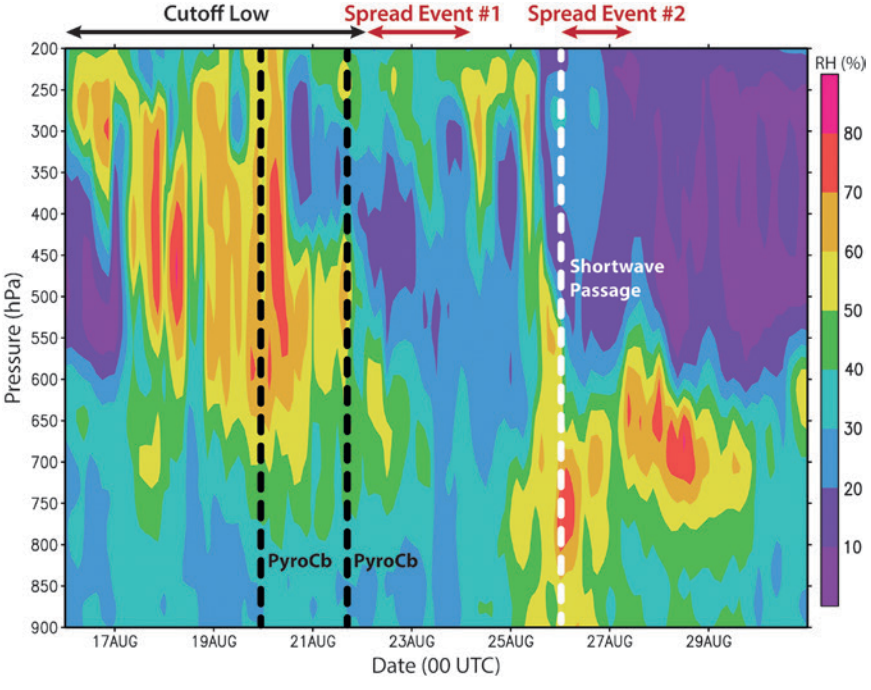

Fig. 9. Vertical profile of NARR RH during the Rim Fire's primary burning period (17–31 Aug) at Crane Flat Lookout. The two pyroCb events (19 and 21 Aug) are denoted by dashed black vertical lines, and the approximate time of the shortwave passage (25 Aug, evening) is donated by the dashed white vertical line.

–7.5°C km^{-1} with plentiful moisture advection in the midtroposphere. Both pyroCbs also coincided with divergence at 250 hPa (negative values). Therefore, the conditions for dry-thunderstorm development were in place.

In combination with upper-level meteorology, several studies have employed traditional stability indices, such as convective available potential energy (CAPE), to estimate the buoyancy available for dry-thunderstorm development (e.g., Peterson et al. 2010; Wallmann et al. 2010) and high-altitude smoke plumes (Potter 2005). The calculation of CAPE is either based on lifting a surface parcel, the most unstable parcel in the lower troposphere (e.g., lowest 300 hPa), or a parcel with the mean properties of the lower troposphere (Bunkers et al. 2002; Wallace and Hobbs 2006). Fromm et al. (2010) show that while the majority of pyroCb events occur with a dry, unstable lower troposphere (high Haines index), the amount of CAPE varies, with several pyroCbs corresponding with little or no CAPE. This is not surprising because dry thunderstorms are rooted in a moist layer well above the surface and no variation of CAPE considers entrainment of the surrounding air (Holton 2004). CAPE calculations also do not account for the increase in buoyancy produced by the intense radiant heat (high FRP) of the fire.

High-based, dry thunderstorms are often triggered by orographic lifting, which is common in the Sierra Nevada during the summer (June–August), and may help explain the presence of nonfire-related convection above ~2200 m (Fig. 10). In the case of the lower-elevation Rim Fire (~915–2100 m), high FRP potentially served as the primary triggering mechanism, producing a robust updraft extending into the layer of ambient midlevel moisture. The pyroCb on 19 August encountered deeper midlevel moisture than the pyroCb on 21 August (Figs. 9, 10), but the duration of high FRP, and therefore smoke plume buoyancy, was higher on 21 August. This suggests that pyroCb development may be possible under marginal dry-thunderstorm conditions if enough buoyancy is generated by the fire.

The remainder of days impacted by the cutoff low (17, 18, and 20 August) either coincided with comparatively less moisture in the midlevels (Fig. 9), unfavorable upper-level dynamics (not shown), or reduced FRP (Fig. 2), which plausibly reconciles why pyroCbs did not occur. The shortwave passage on 25 August between 2100 and 0000 UTC (1400–1700 LT) and the lingering layer of midlevel moisture (26–28 August; Fig. 9) also seemed to produce ideal conditions for pyroCb development. GOES imagery suggests that general pyroCu activity was occurring (Fig. 10) but pyroCbs were not observed. On these dates, central California was either located in the entrance region of a cyclonically curved jet streak or within a broad region of anticyclonic (negative) vorticity advection. As evidenced by 250-hPa convergence in Fig. 10 (25 August), these features are unfavorable for thunderstorm development, presumably including pyroCbs. Therefore, similar to the aforementioned discussion on extreme fire spread, automated prediction of pyroCbs will likely require a top-down approach, based on the collocation of high FRP with favorable upper-level dynamics, midlevel moisture, and a high Haines index environment.

IMPACT OF PYROCBS ON FIRE SPREAD AND PLUME HEIGHT. The pyroCb is an extreme manifestation of a plume-dominated fire, where latent heat release enables the convective column to reach the mid–upper troposphere. In addition, the large aerosol load within a pyroCb yields extremely small cloud droplets, which delays the onset of precipitation and the associated evaporative cooling (Reutter et al. 2014). This may allow a robust updraft to persist for a longer period of time compared with traditional convection, which would feed back as enhanced fire spread. However, the change in FRP during the actual pyroCb event is unknown, because the anvil produced by the pyroCb usually precludes all satellite fire observations. Therefore, while the Rim Fire may help explain the conditions favorable for pyroCb development, the associated short-term impact on a fire spread and FRP is currently unclear.

Previous studies show that the robust updraft within a pyroCb is likely the most efficient avenue to loft recently emitted smoke particles into the upper troposphere, or even the lower stratosphere (e.g., Fromm et al. 2010). The approximate height of a pyroCb can be inferred by matching the cloud-top thermal infrared brightness temperature observed by GOES against the environmental temperature profiles in Fig. 10 (Fromm et al. 2010). During the pyroCb events on 19 and 21 August, the respective minimum cloud-top brightness temperatures reached –60.0° and –35.0°C. This yields respective cloud-top heights of 12.7 km (190 hPa, approximate tropopause height) and 9.6 km (300 hPa).

Upper-tropospheric smoke lofted by both pyroCb events was transported to the northwest, around the cutoff low. Observations from the Cloud–Aerosol Lidar with Orthogonal Polarization (CALIOP), flown aboard NASA's *CALIPSO* satellite (Winker

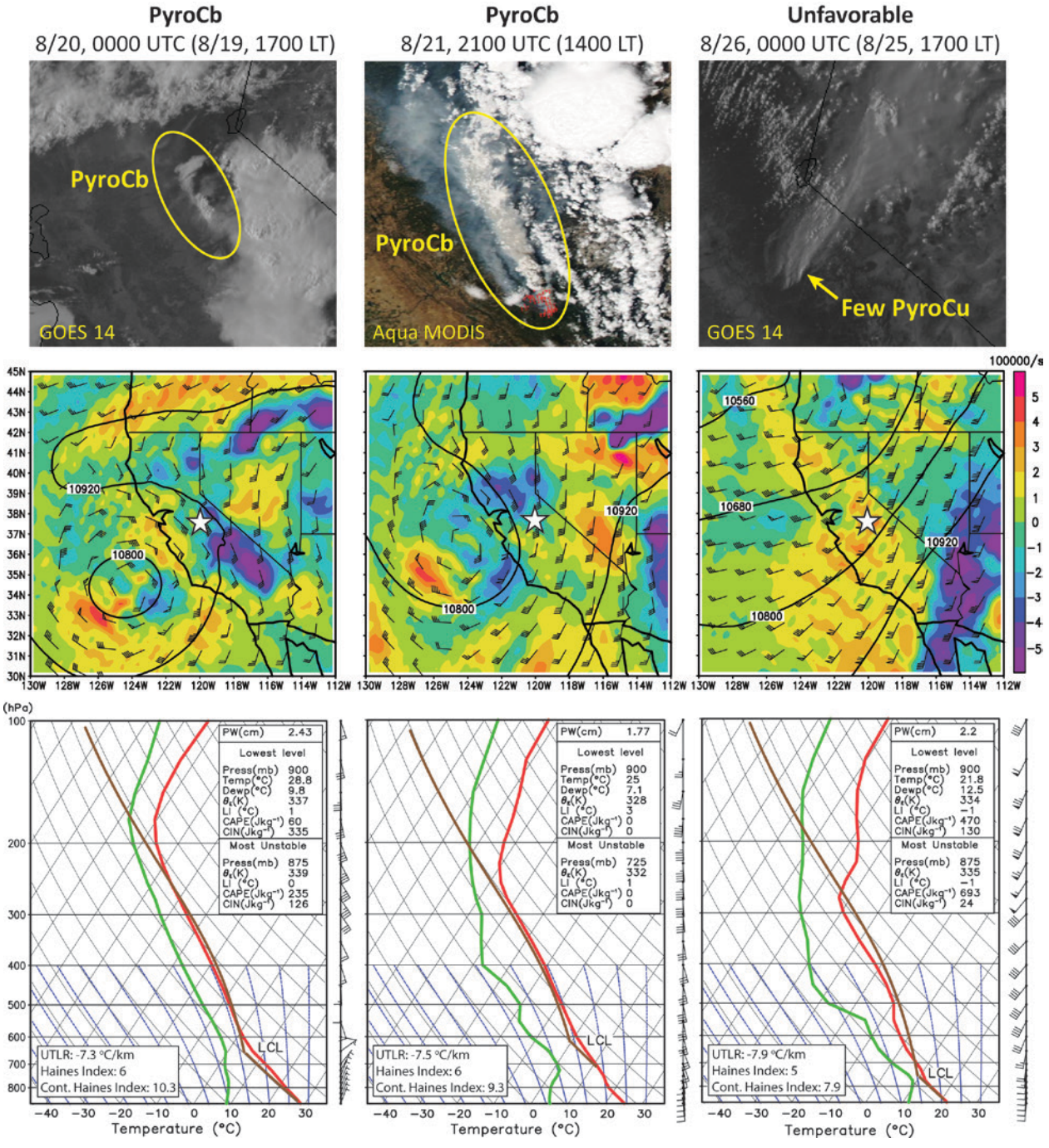

Fig. 10. Atmospheric dynamics and thermodynamics observed during the Rim Fire's two pyroCb events (19 and 21 Aug) and the shortwave passage on 25 Aug. (top) Visible imagery from *GOES-14* (available on 19 and 25 Aug) or MODIS true color image with fire pixels displayed in red. (middle) Corresponding maps of NARR 250-hPa heights (contoured every 120 m) and wind barbs (kt), with horizontal convergence shaded every 1×10^{-5} s^{-1} (negative values indicate divergence). White star denotes the location of the Rim Fire. (bottom) Corresponding soundings derived from the NARR grid box closest to Crane Flat Lookout, with red and green profiles indicating the environmental temperature and dewpoint, respectively. Brown parcel path corresponds to the most unstable parcel.

et al. 2010) are displayed in Fig. 11 for a nighttime overpass beginning at 1039 UTC (0339 LT) 20 August near the Pacific Coast. These attenuated backscatter (km^{-1} sr^{-1}) data reveal areas of aerosol, with clouds embedded, dispersed above the marine boundary layer from 2 to 10 km above mean sea level. Backward

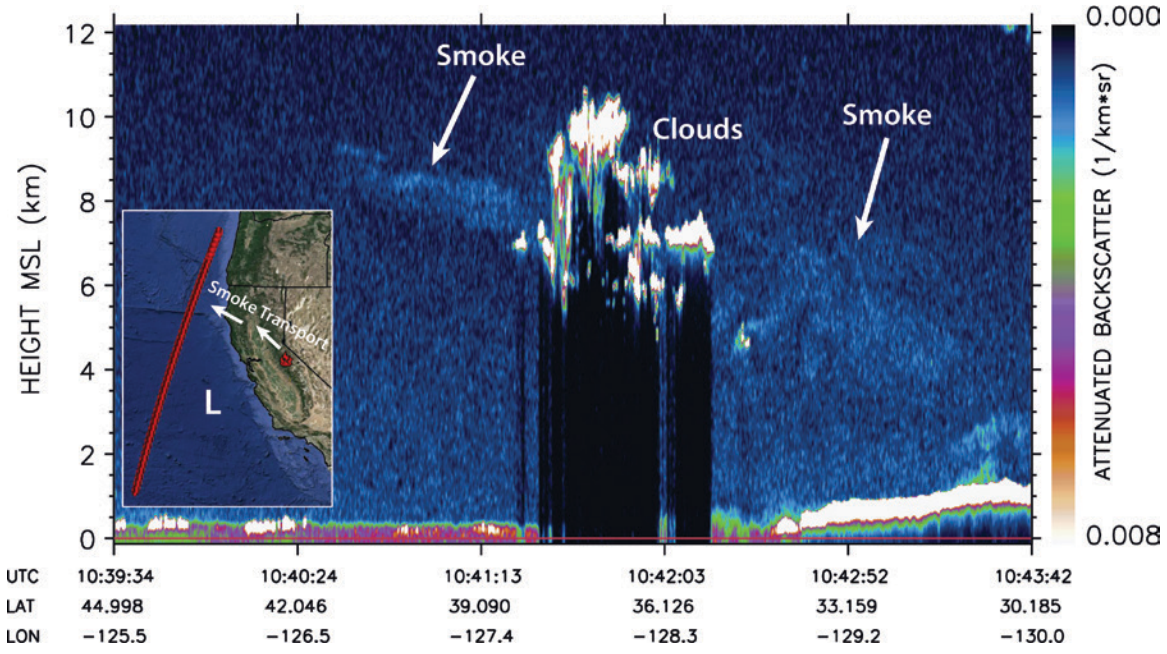

Fig. 11. Attenuated backscatter (km^{-1} sr^{-1}) observed by CALIOP on 20 Aug 2013 for a nighttime (descending) *CALIPSO* overpass beginning 1039 UTC (0339 LT). The inset image displays the path of the *CALIPSO* overpass (red line), the location of the Rim Fire (red symbol), and the approximate smoke transport direction around the cutoff low (white).

trajectories (not shown) show that smoke particles above 8 km likely originated from the 19 August pyroCb. While the Rim Fire's most extreme spread events were also partially plume driven, they occurred in an environment less conducive to pyroCb development and failed to loft smoke above 5 km (Fig. 8). Therefore, while a successful pyroCb prediction may be important for determining the vertical extent of smoke-layer depth over a fire and the associated downwind transport, it may be unable to identify cases of extreme fire spread and high FRP.

SUMMARY AND CONCLUSIONS. A variety of regional fire weather and smoke forecasting applications are currently available to identify air quality, visibility, and societal impacts during large fire events. The most pressing needs for improving these systems are 1) prediction of extreme fire spread and intensity and 2) prediction of high-altitude smoke injection. While these two needs are related, the analysis of the 2013 Rim Fire in central California shows that they are not predicted by the same set of conditions and variables.

The combination of long-term, regional drought and remote terrain set the stage for large fire growth during the Rim Fire. The primary drivers of general fire growth were the interplay of low RH, an unstable lower atmosphere, and strong low-level winds. The surface wind direction relative to the local topography (uphill or downhill) also played an important role. This lower-tropospheric meteorology forms the foundation of the operational fire weather indices currently used to estimate fire danger in North America. However, indices such as the Haines index were unable to identify the most extreme fire behavior during the Rim Fire. As a result, fire weather indices are likely most relevant for forecasting the general growth or decay of fire activity. A top-down approach, beginning with upper-level meteorology, must also be considered when forecasting extreme fire spread and pyroCb development.

Extreme fire spread was initiated as an upper-level disturbance passed over (or near) the fire, and was primarily driven by the corresponding period of sustained low RH and strong near-surface winds, especially during the nighttime hours. PyroCu were observed during both major spread events, but were unable to develop into a pyroCb likely because of a dry atmospheric column and/or unfavorable upper-level dynamics. In addition, the high FRP observed during the major spread events failed to generate enough buoyancy to loft smoke particles to the altitudes commonly reached during a large pyroCb event.

In contrast, the Rim Fire's two pyroCb events, and therefore the highest direct injection altitude

of smoke particles, occurred well ahead of an approaching upper-level disturbance (cutoff low), in an environment favorable for midlevel moisture entrainment and upper-level instability. Therefore, the observational approach of this analysis supports the results of several modeling studies (e.g., Trentmann et al. 2006; Luderer et al. 2009), by showing that ambient midlevel moisture likely has an important role in pyroCb development. In addition, this analysis suggests that the meteorological environment commonly associated with high-based, dry thunderstorms in the southwestern CONUS is likely a general precursor for pyroCbs, especially in the presence of a large and intense fire.

Several operational fire weather and smoke forecasting applications are automated, and therefore rely on a continuous source of NWP and satellite fire observations (e.g., Peterson et al. 2013a). As a result, only a small subset of meteorological variables and indices may be practical when predicting smoke emissions at broad spatial scales. Satellite fire data have their own set of limitations, primarily from the coarse spatial resolution of data sources that provide at least one observation per day. However, spatially uniform fire data at resolutions of 375 and 750 m are now becoming available from the Visible Infrared Imaging Radiometer Suite aboard the *Suomi National Polar-Orbiting Partnership* (*S-NPP*/VIIRS; Coen and Schroeder 2013; Hillger et al. 2013; Csiszar et al. 2014; Schroeder et al. 2014). Recent studies have also shown that radiant energy flux over the fire area can be calculated based on retrieved subpixel instantaneous fire area and temperature (Peterson and Wang 2013; Peterson et al. 2013b), which may result in an improved characterization of smoke plume injection heights (Peterson et al. 2014). Therefore, the combination of meteorology from numerical forecast models and improved exploitation of satellite observations has great potential for improving automated regional forecasts of fire behavior and smoke production, especially in remote areas where detailed observations are unavailable.

ACKNOWLEDGMENTS. We thank Ralph Kahn (NASA Goddard), Jeffrey Reid (Naval Research Laboratory), Bob Yokelson (University of Montana), and the National Weather Service in Monterey, California, for their helpful advice. We are all grateful to Shelly Crook at the Stanislaus National Forest Service, as well as Mark Schug, Brad Quayle, and many other USFS employees for providing the NIROPS fire perimeter data used in this study. We also acknowledge contributions from the NASA SEAC^{4}RS Science Team, especially the DIAL/HSRL lidar group, project scientist Brian Toon, and project managers Hal Maring and Kenneth Jucks. This research was performed while David Peterson held a National Research Council Research Associateship Award at the Naval Research Laboratory. Edward Hyer's contributions were supported by the NASA SEAC^{4}RS program under NASA Award NNH12AT27i. James Campbell acknowledges the support of NASA Interagency Agreement NNG13HH10I, on behalf of the Micro Pulse Lidar Network and SEAC^{4}RS Science Team.

REFERENCES

Amiro, B. D., K. A. Logan, B. M. Wotton, M. D. Flannigan, J. B. Todd, B. J. Stocks, and D. L. Martell, 2004: Fire weather index system components for large fires in the Canadian boreal forest. *Int. J. Wildland Fire,* **13,** 391–400, doi:10.1071/WF03066.

Brotak, E. A., and W. E. Reifsnyder, 1977: Investigation of synoptic situations associated with major wildland fires. *J. Appl. Meteor.,* **16,** 867–870, doi:10.1175/1520-0450(1977)016<0867:AIOTSS>2.0.CO;2.

Browell, E. V., S. Ismail, and W. B. Grant, 1998: Differential absorption lidar (DIAL) measurements from air and space. *Appl. Phys.,* **67B,** 399–410, doi:10.1007/s003400050523.

Bunkers, M. J., B. A. Klimowski, and J. W. Zeitler, 2002: The importance of parcel choice and the measure of vertical wind shear in evaluating the convective environment. *21st Conf. on Severe Local Storms,* San Antonio, TX, Amer. Meteor. Soc., P8.2. [Available online at https://ams.confex.com/ams/SLS_WAF_NWP/techprogram/paper_47319.htm.]

Coen, J. L., and W. Schroeder, 2013: Use of spatially refined satellite remote sensing fire detection data to initialize and evaluate coupled weather-wildfire growth model simulations. *Geophys. Res. Lett.,* **40,** 5536–5541, doi:10.1002/2013GL057868.

Csiszar, I., W. Schroeder, L. Giglio, E. Ellicott, K. P. Vadrevu, C. O. Justice, and B. Wind, 2014: Active fires from the Suomi NPP Visible Infrared Imaging Radiometer Suite: Product status and first evaluation results. *J. Geophys. Res. Atmos.,* **119,** 803–816, doi:10.1002/2013JD020453.

Cunningham, P., and M. J. Reeder, 2009: Severe convective storms initiated by intense wildfires: Numerical simulations of pyro-convection and pyro-tornadogenesis. *Geophys. Res. Lett.,* **36,** L12812, doi:10.1029/2009GL039262.

Damoah, R., and Coauthors, 2006: A case study of pyro-convection using transport model and remote sensing data. *Atmos. Chem. Phys.,* **6,** 173–185, doi:10.5194/acp-6-173-2006.

Dempsey, F., 2013: Forest fire effects on air quality in Ontario: Evaluation of several recent examples. *Bull. Amer. Meteor. Soc.,* **94,** 1059–1064, doi:10.1175/BAMS-D-11-00202.1.

Dennison, P. E., S. C. Brewer, J. D. Arnold, and M. A. Moritz, 2014: Large wildfire trends in the western United States, 1984–2011. *Geophys. Res. Lett.,* **41,** 2928–2933, doi:10.1002/2014GL059576.

Draxler, R. R., and G. D. Rolph, cited 2014: HYSPLIT—Hybrid Single Particle Lagrangian Integrated Trajectory model. [Available online at www.arl.noaa.gov/HYSPLIT.php.]

Duck, T. J., and Coauthors, 2007: Transport of forest fire emissions from Alaska and the Yukon Territory to Nova Scotia during summer 2004. *J. Geophys. Res.,* **112,** D10S44, doi:10.1029/2006JD007716.

Flannigan, M. D., and J. B. Harrington, 1988: A study of the relation of meteorological variables to monthly provincial area burned by wildfire in Canada (1953–80). *J. Appl. Meteor.,* **27,** 441–452, doi:10.1175/1520-0450(1988)027<0441:ASOTRO>2.0.CO;2.

Fromm, M. D., D. T. Lindsey, R. Servranckx, G. Yue, T. Trickl, R. Sica, P. Doucet, and S. Godin-Beekmann, 2010: The untold story of pyrocumulonimbus. *Bull. Amer. Meteor. Soc.,* **91,** 1193–1209, doi:10.1175/2010BAMS3004.1.

——, R. H. D. McRae, J. J. Sharples, and G. P. Kablick III, 2012: Pyrocumulonimbus pair in Wollemi and Blue Mountains National Parks, 22 November 2006. *Aust. Meteor. Oceanogr. J.,* **62,** 117–126.

Giglio, L., 2007: Characterization of the tropical diurnal fire cycle using VIRS and MODIS observations. *Remote Sens. Environ.,* **108,** 407–421, doi:10.1016/j.rse.2006.11.018.

——, 2010: MODIS collection 5 active fire product user's guide, version 2.4. University of Maryland, Dept. of Geography, 61 pp.

——, J. Descloitres, C. O. Justice, and Y. J. Kaufman, 2003: An enhanced contextual fire detection algorithm for MODIS. *Remote Sens. Environ.,* **87,** 273–282, doi:10.1016/S0034-4257(03)00184-6.

——, I. Csiszar, and C. O. Justice, 2006: Global distribution and seasonality of active fires as observed with the Terra and Aqua Moderate Resolution Imaging Spectroradiometer (MODIS) sensors. *J. Geophys. Res.,* **111,** G02016, doi:10.1029/2005JG000142.

Haines, D. A., 1988: A lower atmosphere severity index for wildland fires. *Natl. Wea. Dig.,* **13** (2), 23–27.

Hair, J. W., and Coauthors, 2008: Airborne High Spectral Resolution Lidar for profiling aerosol optical properties. *Appl. Opt.,* **47,** 6734–6752, doi:10.1364/AO.47.006734.

Heward, H., A. M. S. Smith, D. P. Roy, W. T. Tinkham, C. M. Hoffman, P. Morgan, and K. O. Lannom, 2013: Is burn severity related to fire intensity? Observations from landscape scale remote sensing. *Int. J. Wildland Fire,* **22,** 910–918, doi:10.1071/WF12087.

Hillger, D., and Coauthors, 2013: First-light imagery from Suomi NPP VIIRS. *Bull. Amer. Meteor. Soc.,* **94,** 1019–1029, doi:10.1175/BAMS-D-12-00097.1.

Holton, J. R., 2004: *An Introduction to Dynamic Meteorology.* 4th ed. International Geophysics Series, Vol. 88, Academic Press, 535 pp.

Hyer, E. J., E. S. Kasischke, and D. J. Allen, 2007: Effects of source temporal resolution on transport simulations of boreal fire emissions. *J. Geophys. Res.,* **112,** D01302, doi:10.1029/2006JD007234.

——, J. S. Reid, E. M. Prins, J. P. Hoffman, C. C. Schmidt, J. I. Miettinen, and L. Giglio, 2013: Patterns of fire activity over Indonesia and Malaysia from polar and geostationary satellite observations. *Atmos. Res.,* **122,** 504–519, doi:10.1016/j.atmosres.2012.06.011.

Ichoku, C., and Y. J. Kaufman, 2005: A method to derive smoke emission rates from MODIS fire radiative energy measurements. *IEEE Trans. Geosci. Remote Sens.,* **43,** 2636–2649, doi:10.1109/TGRS.2005.857328.

——, L. Giglio, M. J. Wooster, and L. A. Remer, 2008a: Global characterization of biomass-burning patterns using satellite measurements of fire radiative energy. *Remote Sens. Environ.,* **112,** 2950–2962, doi:10.1016/j.rse.2008.02.009.

——, and Coauthors, 2008b: Laboratory investigation of fire radiative energy and smoke aerosol emissions. *J. Geophys. Res.,* **113,** D14S09, doi:10.1029/2007JD009659.

Johnson, M., S. Crook, M. Stuart, and M. Romero, 2013: Rim Fire—Preliminary fuel treatment effectiveness report. USDA Forest Service Rep., 7 pp. [Available online at www.fs.usda.gov/Internet/FSE_DOCUMENTS/stelprdb5436551.pdf.]

Jordan, N. S., C. Ichoku, and R. M. Hoff, 2008: Estimating smoke emissions over the US Southern Great Plains using MODIS fire radiative power and aerosol observations. *Atmos. Environ.,* **42,** 2007–2022, doi:10.1016/j.atmosenv.2007.12.023.

Kahn, R. A., W.-H. Li, C. Moroney, D. J. Diner, J. V. Martonchik, and E. Fishbein, 2007: Aerosol source plume physical characteristics from space-based multiangle imaging. *J. Geophys. Res.,* **112,** D11205, doi:10.1029/2006JD007647.

——, Y. Chen, D. L. Nelson, F.-Y. Leung, Q. Li, D. J. Diner, and J. A. Logan, 2008: Wildfire smoke injection heights: Two perspectives from space. *Geophys. Res. Lett.,* **35,** L04809, doi:10.1029/2007GL032165.

Kaiser, J. W., and Coauthors, 2012: Biomass burning emissions estimated with a global fire assimilation system based on observed fire radiative power.

Biogeosciences, **9,** 527–554, doi:10.5194/bg-9-527-2012.

Kaufman, Y. J., and Coauthors, 1998: Potential global fire monitoring from EOS-MODIS. *J. Geophys. Res.,* **103,** 32 215–32 238, doi:10.1029/98JD01644.

Kirn, L., and G. Dickman, 2013: Yosemite NP Rim Fire 2013—Burned area emergency response plan. National Park Service Rep., 99 pp. [Available online at www.nps.gov/yose/parkmgmt/upload/RIM_BAER_PLAN2013.pdf.]

Larkin, N. K., and Coauthors, 2009: The BlueSky smoke modeling framework. *Int. J. Wildland Fire,* **18,** 906–920, doi:10.1071/WF07086.

Luderer, G., J. Trentmann, and M. O. Andreae, 2009: A new look at the role of fire-released moisture on the dynamics of atmospheric pyro-convection. *Int. J. Wildland Fire,* **18,** 554–562, doi:10.1071/WF07035.

Mesinger, F., and Coauthors, 2006: North American Regional Reanalysis. *Bull. Amer. Meteor. Soc.,* **87,** 343–360, doi:10.1175/BAMS-87-3-343.

Mills, G. A., and L. McCaw, 2010: Atmospheric stability environments and fire weather in Australia—Extending the Haines index. CAWCR Tech. Rep. 20, 158 pp.

Mölders, N., 2008: Suitability of the Weather Research and Forecasting (WRF) Model to predict the June 2005 fire weather for interior Alaska. *Wea. Forecasting,* **23,** 953–973, doi:10.1175/2008WAF2007062.1.

Mu, M., and Coauthors, 2011: Daily and 3-hourly variability in global fire emissions and consequences for atmospheric model predictions of carbon monoxide. *J. Geophys. Res.,* **116,** D24303, doi:10.1029/2011JD016245.

Nauslar, N. J., M. L. Kaplan, J. Wallmann, and T. J. Brown, 2013: A forecast procedure for dry thunderstorms. *J. Oper. Meteor.,* **1,** 200–214, doi:10.15191/nwajom.2013.0117.

Peterson, D., and J. Wang, 2013: A sub-pixel-based calculation of fire radiative power from MODIS observations: 2. Sensitivity analysis and potential fire weather application. Remote Sensing of Environment, 129, 231-249.

——, ——, C. Ichoku, and L. A. Remer, 2010: Effects of lightning and other meteorological factors on fire activity in the North American boreal forest: Implications for fire weather forecasting. *Atmos. Chem. Phys.,* **10,** 6873–6888, doi:10.5194/acp-10-6873-2010.

——, E. Hyer, and J. Wang, 2013a: A short-term predictor of satellite-observed fire activity in the North American boreal forest: Toward improving the prediction of smoke emissions. *Atmos. Environ.,* 71, 304-310.

——, J. Wang, C. Ichoku, E. Hyer, and V. Ambrosia, 2013b: A sub-pixel-based calculation of fire radiative power from MODIS observations. 1: Algorithm development and initial assessment. *Remote Sens. Environ.,* **129,** 262–279, doi:10.1016/j.rse.2012.10.036.

——, E. Hyer, and J. Wang, 2014: Quantifying the potential for high-altitude smoke injection in the North American boreal forest using the standard MODIS fire products and subpixel-based methods. Journal of Geophysical Research: Atmospheres, 119, 2013JD021067.

Potter, B. E., 2005: The role of released moisture in the atmospheric dynamics associated with wildland fires. *Int. J. Wildland Fire,* **14,** 77–84, doi:10.1071/WF04045.

——, J. A. Winkler, D. F. Wilhelm, and R. P. Shadbolt, 2008: Computing the low-elevation variant of the Haines index for fire weather forecasts. *Wea. Forecasting,* **23,** 159–167, doi:10.1175/2007WAF2007025.1.

Prins, E. M., and W. P. Menzel, 1994: Trends in South American biomass burning detected with the GOES visible infrared spin scan radiometer atmospheric sounder from 1983 to 1991. *J. Geophys. Res.,* **99,** 16 719–16 735, doi:10.1029/94JD01208.

——, J. M. Feltz, W. P. Menzel, and D. E. Ward, 1998: An overview of GOES-8 diurnal fire and smoke results for SCAR-B and 1995 fire season in South America. *J. Geophys. Res.,* **103,** 31 821–31 835, doi:10.1029/98JD01720.

Randerson, J. T., and Coauthors, 2006: The impact of boreal forest fire on climate warming. *Science,* **314,** 1130–1132, doi:10.1126/science.1132075.

Reid, J. S., and Coauthors, 2009: Global monitoring and forecasting of biomass-burning smoke: Description of and lessons from the Fire Locating and Modeling of Burning Emissions (FLAMBE) Program. *IEEE J. Sel. Top. Appl. Earth Obs. Remote Sens.,* **2,** 144–162, doi:10.1109/JSTARS.2009.2027443.

Remer, L. A., and Coauthors, 2005: The MODIS aerosol algorithm, products, and validation. *J. Atmos. Sci.,* **62,** 947–973, doi:10.1175/JAS3385.1.

Reutter, P., and Coauthors, 2014: 3-D model simulations of dynamical and microphysical interactions in pyroconvective clouds under idealized conditions. *Atmos. Chem. Phys.,* **14,** 7573–7583, doi:10.5194/acp-14-7573-2014.

Roberts, G., M. J. Wooster, G. L. W. Perry, N. Drake, L.-M. Rebelo, and F. Dipotso, 2005: Retrieval of biomass combustion rates and totals from fire radiative power observations: Application to southern Africa using geostationary SEVIRI imagery. *J. Geophys. Res.,* **110,** D21111, doi:10.1029/2005JD006018.

——, ——, and E. Lagoudakis, 2009: Annual and diurnal African biomass burning temporal dynamics. *Biogeosciences,* **6,** 849–866, doi:10.5194/bg-6-849-2009.

Rorig, M. L., and S. A. Ferguson, 1999: Characteristics of lightning and wildland fire ignition in the Pacific Northwest. *J. Appl. Meteor.,* **38,** 1565–1575, doi:10.1175/1520-0450(1999)038<1565:COLAWF>2.0.CO;2.

Rothermel, R. C., 1991: Predicting behavior and size of crown fires in the northern Rocky Mountains. USDA Forest Service, Intermountain Research Station, Research Paper INT-438, 46 pp. [Available online at http://digitalcommons.usu.edu/cgi/viewcontent.cgi?article=1064&context=barkbeetles.]

Salinas, S. V., B. N. Chewa, J. Miettinen, J. R. Campbell, E. J. Welton, J. S. Reidd, L. E. Yue, and S. C. Liew, 2013: Physical and optical characteristics of the October 2010 haze event over Singapore: A photometric and lidar analysis. *Atmos. Res.,* **122,** 555–570, doi:10.1016/j.atmosres.2012.05.021.

Sapkota, A., and Coauthors, 2005: Impact of the 2002 Canadian forest fires on particulate matter air quality in Baltimore City. *Environ. Sci. Technol.,* **39,** 24–32, doi:10.1021/es035311z.

Schroeder, W., I. Csiszar, L. Giglio, and C. C. Schmidt, 2010: On the use of fire radiative power, area, and temperature estimates to characterize biomass burning via moderate to coarse spatial resolution remote sensing data in the Brazilian Amazon. *J. Geophys. Res.,* **115,** D21121, doi:10.1029/2009JD013769.

——, P. Oliva, L. Giglio, and I. A. Csiszar, 2014: The New VIIRS 375 m active fire detection data product: Algorithm description and initial assessment. *Remote Sens. Environ.,* **143,** 85–96, doi:10.1016/j.rse.2013.12.008.

Simpson, C. C., H. G. Pearce, A. P. Sturman, and P. Zawar-Reza, 2014: Verification of WRF modelled fire weather in the 2009–10 New Zealand fire season. *Int. J. Wildland Fire,* **23,** 34–45, doi:10.1071/WF12152.

Snellman, L. W., 1982: Impact of AFOS on operational forecasting. Preprints, *Ninth Conf. on Weather Forecasting and Analysis*, Seattle, WA, Amer. Meteor. Soc., 13–16.

Spracklen, D. V., J. A. Logan, L. J. Mickley, R. J. Park, R. Yevich, A. L. Westerling, and D. A. Jaffe, 2007: Wildfires drive interannual variability of organic carbon aerosol in the western U.S. in summer. *Geophys. Res. Lett.,* **34,** L16816, doi:10.1029/2007GL030037.

Trentmann, J., and Coauthors, 2006: Modeling of biomass smoke injection into the lower stratosphere by a large forest fire (Part I): Reference simulation. *Atmos. Chem. Phys.,* **6,** 5247–5260, doi:10.5194/acp-6-5247-2006.

Val Martin, M., J. A. Logan, R. A. Kahn, F. Y. Leung, D. L. Nelson, and D. J. Diner, 2010: Smoke injection heights from fires in North America: Analysis of 5 years of satellite observations. *Atmos. Chem. Phys.,* **10,** 1491–1510, doi:10.5194/acp-10-1491-2010.

——, R. A. Kahn, J. A. Logan, R. Paugam, M. Wooster, and C. Ichoku, 2012: Space-based observational constraints for 1-D fire smoke plume-rise models. *J. Geophys. Res.,* **117,** D22204, doi:10.1029/2012JD018370.

——, C. L. Heald, B. Ford, A. J. Prenni, and C. Wiedinmyer, 2013: A decadal satellite analysis of the origins and impacts of smoke in Colorado. *Atmos. Chem. Phys.,* **13,** 7429–7439, doi:10.5194/acp-13-7429-2013.

van der Werf, G. R., and Coauthors, 2010: Global fire emissions and the contribution of deforestation, savanna, forest, agricultural, and peat fires (1997–2009). *Atmos. Chem. Phys.,* **10,** 11 707–11 735, doi:10.5194/acp-10-11707-2010.

Van Wagner, C. E., 1987: Development and structure of the Canadian Forest Fire Weather Index System. Canadian Forestry Service Forestry Tech. Rep. 35, 37 pp.

Wallace, J. M., and P. V. Hobbs, 2006: *Atmospheric Science: An Introductory Survey.* 2nd ed. International Geophysics Series, Vol. 92, Academic Press, 483 pp.

Wallmann, J., R. Milne, C. Smallcomb, and M. Mehle, 2010: Using the 21 June 2008 California lightning outbreak to improve dry lightning forecast procedures. *Wea. Forecasting,* **25,** 1447–1462, doi:10.1175/2010WAF2222393.1.

Wang, J., S. A. Christopher, U. S. Nair, J. S. Reid, E. M. Prins, J. Szykman, and J. L. Hand, 2006: Mesoscale modeling of Central American smoke transport to the United States: 1. "Top-down" assessment of emission strength and diurnal variation impacts. *J. Geophys. Res.,* **111,** D05S17, doi:10.1029/2005JD006416.

——, and Coauthors, 2013: Mesoscale modeling of smoke transport over the Southeast Asian Maritime Continent: Interplay of sea breeze, trade wind, typhoon, and topography. *Atmos. Res.,* **122,** 486–503, doi:10.1016/j.atmosres.2012.05.009.

Werth, P., and R. Ochoa, 1993: The evaluation of Idaho wildfire growth using the Haines index. *Wea. Forecasting,* **8,** 223–234, doi:10.1175/1520-0434(1993)008<0223:TEOIWG>2.0.CO;2.

Westerling, A. L., H. G. Hidalgo, D. R. Cayan, and T. W. Swetnam, 2006: Warming and earlier spring increase western U.S. forest wildfire activity. *Science,* **313,** 940–943, doi:10.1126/science.1128834.

Westphal, D. L., and O. B. Toon, 1991: Simulations of microphysical, radiative, and dynamical processes in a

continental-scale forest fire smoke plume. *J. Geophys. Res.,* **96,** 22 379–22 400, doi:10.1029/91JD01956.

Wiedinmyer, C., S. K. Akagi, R. J. Yokelson, L. K. Emmons, J. A. Al-Saadi, J. J. Orlando, and A. J. Soja, 2011: The Fire Inventory from NCAR (FINN): A high resolution global model to estimate the emissions from open burning. *Geosci. Model Dev.,* **4,** 625–641, doi:10.5194/gmd-4-625-2011.

Winker, D. M., and Coauthors, 2010: The CALIPSO mission: A global 3D view of aerosols and clouds. *Bull. Amer. Meteor. Soc.,* **91,** 1211–1229, doi:10.1175/2010BAMS3009.1.

Wooster, M. J., 2002: Small-scale experimental testing of fire radiative energy for quantifying mass combusted in natural vegetation fires. *Geophys. Res. Lett.,* **29,** 2027, doi:10.1029/2002GL015487.

——, B. Zhukov, and D. Oertel, 2003: Fire radiative energy for quantitative study of biomass burning: Derivation from the BIRD experimental satellite and comparison to MODIS fire products. *Remote Sens. Environ.,* **86,** 83–107, doi:10.1016/S0034-4257(03)00070-1.

——, G. Roberts, G. L. W. Perry, and Y. J. Kaufman, 2005: Retrieval of biomass combustion rates and totals from fire radiative power observations: FRP derivation and calibration relationships between biomass consumption and fire radiative energy release. *J. Geophys. Res.,* **110,** D24311, doi:10.1029/2005JD006318.

Wotawa, G., and M. Trainer, 2000: The influence of Canadian forest fires on pollutant concentrations in the United States. *Science,* **288,** 324–328, doi:10.1126/science.288.5464.324.

Zhang, X., S. Kondragunta, C. Schmidt, and F. Kogan, 2008: Near real time monitoring of biomass burning particulate emissions (PM2.5) across contiguous United States using multiple satellite instruments. *Atmos. Environ.,* **42,** 6959–6972, doi:10.1016/j.atmosenv.2008.04.060.

——, ——, J. Ram, C. C. Schmidt, and H.-C. Huang, 2012: Near-real-time global biomass burning emissions product from geostationary satellite constellation. *J. Geophys. Res.,* **117,** D14201, doi:10.1029/2012JD017459.

Science at Your Fingertips

AMS Journals are now optimized for viewing on your mobile device.

Access journal articles, monograph titles, and BAMS content using your iOS, Android, or Blackberry phone, or tablet.

Features include:

- **Saving articles for offline reading**
- **Sharing of article links via email and social networks**
- **Searching across journals, authors, and keywords**

And much more...

Scan code to connect to journals.ametsoc.org

AMERICAN METEOROLOGICAL SOCIETY